nature energy

Article

https://doi.org/10.1038/s41560-025-01857-y

Designing an isotropic epilayer for stable 4.2 V solid-state Na batteries

Received: 14 May 2024

Accepted: 6 August 2025

Published online: 05 September 2025

Check for updates

Yuan Liu[1,2,8], Huican Mao[3,8], Rui Bai[1], Suting Weng[1], Qiangqiang Zhang[1], Xiaohui Rong[4] ✉, Xiao Chen[5], Chu Zhang[1], Shuai Han[1], Feixiang Ding[1], Xuefeng Wang[1], Yaxiang Lu[1,6] ✉, Junmei Zhao[7] ✉, Fei Wei[5], Liquan Chen[1] & Yong-Sheng Hu[1,2,6] ✉

Side reactions between high-voltage cathodes and electrolytes remain a critical obstacle to the advancement of solid-state batteries—particularly for Na-ion systems—due to the higher Na^+/Na redox potential. Despite recent extensive efforts, achieving a long cycle life is still challenging at the 4.2 V cut-off (versus Na^+/Na). Here we design a room-temperature isotropic epitaxial growth to achieve a relatively uniform and dense metal–organic framework epilayer on $Na_3V_2O_2(PO_4)_2F$ surfaces. Despite using polyethylene oxide, a typical ether-based solid polymer electrolyte, the cathode with isotropic epilayer exhibits enhanced cycling performance at the 4.2 V cut-off (retaining up to 77.9% of its initial capacity after 1,500 cycles). Combining experimental measurements and theoretical analyses, the key factor governing isotropic epitaxial growth behaviour is explicitly elucidated. Furthermore, we develop a self-designed high-sensitivity characterization method, in situ linear sweep voltammetry coupled with gas chromatography–mass spectrometry, to elucidate the failure mechanism of polyethylene oxide on $Na_3V_2O_2(PO_4)_2F$ surfaces and and to reveal the excellent electrochemical stability of the isotropic epilayer. Interestingly, the universality of this approach has also been validated, highlighting its strong potential as an effective strategy for enabling high-energy-density batteries.

The growing demand for high energy density and enhanced safety has spurred intensive research into all-solid-state batteries, with solid-state sodium batteries emerging as a more cost-effective option due to the abundance of sodium[1–3]. Among alternative solid-state electrolyte materials, solid polymer electrolytes are distinguished by their low cost, high stability, rich resources and relatively soft nature—attributes that are consistent with the needs of large-scale energy storage applications[4]. Nonetheless, they have so far been excluded from high-voltage battery systems due to their limited oxidative stability[5–7]. In addition, the standard electrode potential of Na^+/Na is ~0.3 V higher than that of Li^+/Li, meaning that, to achieve a 4.2 V operating voltage in Na-ion systems, cathode potentials of up to ~4.5 V versus Li^+/Li are needed. Therefore, realizing prolonged cycling stability in high-voltage solid-state Na batteries has remained an intractable challenge[8,9].

The formation of a robust cathode–electrolyte interphase (CEI) is crucial to mitigating continuous side reactions between the

[1]Beijing National Laboratory for Condensed Matter Physics, Institute of Physics, Chinese Academy of Sciences, Beijing, China. [2]College of Materials Science and Optoelectronic Technology, University of Chinese Academy of Sciences, Beijing, China. [3]Department of Materials Science and Key Laboratory of Automobile Materials, MOE, Jilin University, Changchun, China. [4]Yangtze River Delta Physics Research Center Co. Ltd, Liyang, China. [5]Beijing Key Laboratory of Green Chemical Reaction Engineering and Technology, Department of Chemical Engineering, Tsinghua University, Beijing, China. [6]Huairou Division, Institute of Physics, Chinese Academy of Sciences, Beijing, China. [7]CAS Key Laboratory of Green Process and Engineering, Institute of Process Engineering, Chinese Academy of Sciences, Beijing, China. [8]These authors contributed equally: Yuan Liu, Huican Mao.
✉e-mail: rongxiaohui@ioply.cn; yxlu@iphy.ac.cn; jmzhao@ipe.ac.cn; yshu@iphy.ac.cn

https://doi.org/10.1038/s41560-025-01857-y

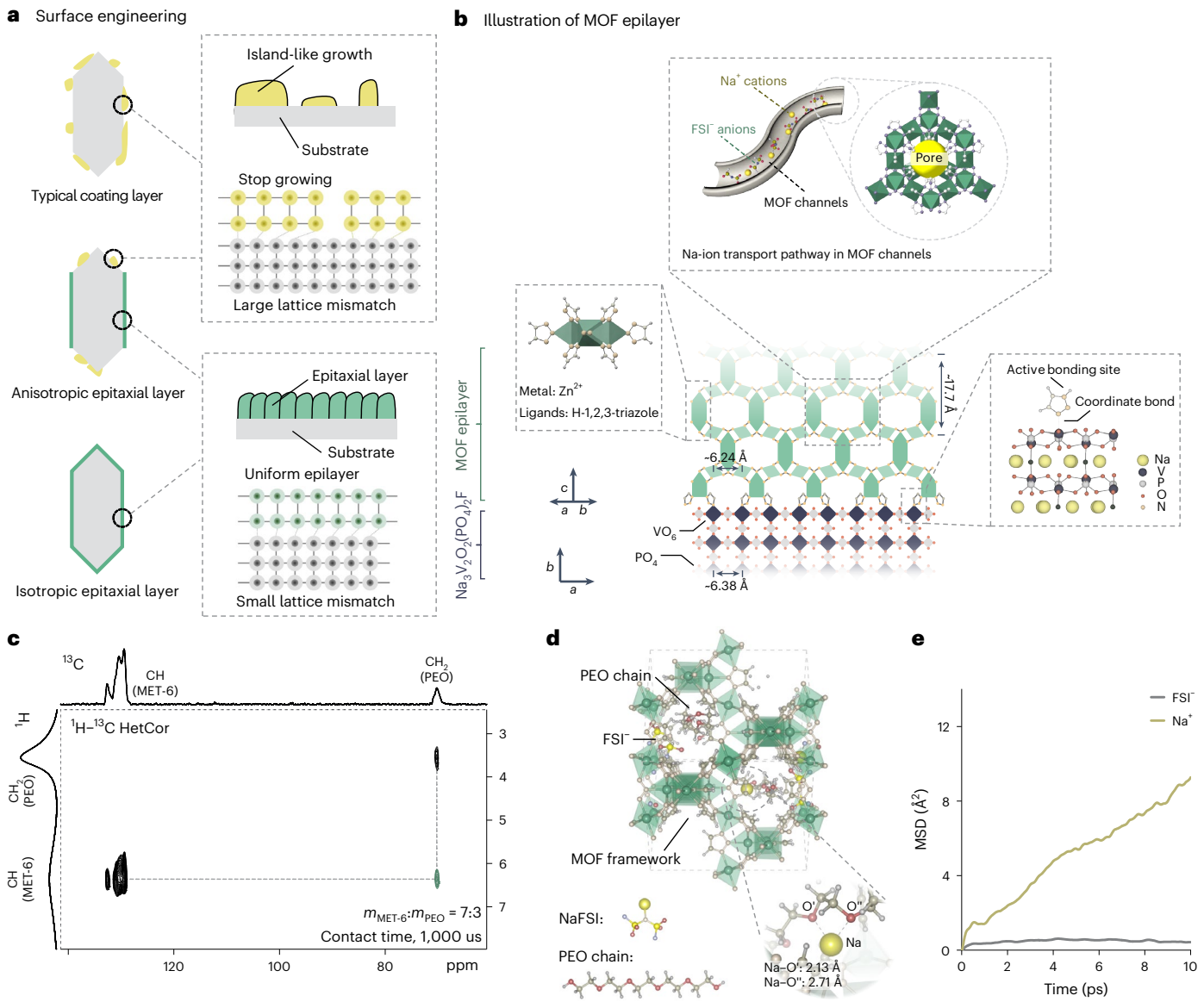

Fig. 1 | Schematics of the surface engineering and Na^+ transport mechanism. **a**, A schematic illustration comparing growth behaviours of conventional coating layers, anisotropic epilayers and isotropic epilayers. **b**, A schematic illustration of the MOF epilayer design. MOF epilayer is triggered by the ligand, which is adsorbed on the NVOPF surface[22,45,46]. As the solid-state electrolyte, MOF provides the Na^+ transport pathway. The lattice parameters shown are based on XRD refinement results. **c**, ^1H–^{13}C HetCor NMR spectrum of MET-6 treated with PEO. **d**, Snapshots from AIMD trajectories at $t = 10$ ps. The enlarged view highlights dynamic Na–O bonds. Zn, green; Na, orange; S, light yellow; O, red; C, brown; F, blue; H, light grey. **e**, The corresponding MSD curves.

cathode and electrolyte under high-voltage conditions[10]. Although extensive research efforts have been devoted to modifying or rebuilding the CEI, the capacity fading remains obvious[11–13]. Notably, lattice mismatch-induced stress accumulation causes the coating layer to manifest as isolated islands on the cathode surface, resulting in continuous electrolyte decomposition at exposed domains[14] (Fig. 1a). Fortunately, epitaxial growth emerges as an appealing surface engineering strategy to construct dense, uniform and electrochemically stable artificial CEI layers[13,15]. However, the crystal anisotropy engenders facet-selective epitaxial growth behaviour, yielding uniform epilayers solely on specific facets while leaving others incompletely coated (Fig. 1a). Therefore, demonstrating and elucidating strategies that facilitate isotropic epitaxial growth on cathode surfaces is imperative for enhancing high-voltage cycling stability.

In this work, we achieved an isotropic epitaxial growth of the metal–organic framework (MOF) layer on $Na_3V_2O_2(PO_4)_2F$ (NVOPF) surfaces at room temperature and illustrated key insights into tailoring isotropic versus anisotropic epitaxial growth modes (Fig. 1a,b). The epilayer self-assembles on the cathode surface, remaining stable during cycling; meanwhile, it increases the operating voltage of polyethylene oxide (PEO)-based electrolyte from 3.87 V to 4.27 V (versus Na^+/Na), which was validated by in situ linear sweep voltammetry coupled with gas chromatography–mass spectrometry (LSV–GCMS). In addition, the rationally designed MOF exhibits considerable ionic conductivity due to its accessible pores and open channels[16–18] (Fig. 1b–d). As a result, NVOPF with MET-6 [$Zn(C_2N_3H_2)_2$] epilayer (denoted as NVOPF@MET) showed a high rate performance and long lifetime, even at a cut-off voltage as high as 4.2 V.

Isotropic epitaxial growth of the MOF epilayer

Epilayer growth follows the path of minimum energy resistance. To achieve an isotropic epilayer, the lattice deformation energy should be relatively low across the entire exposed cathode surface. Notably, MOFs present promising solutions due to their open framework structure,

which results in low lattice deformation energy[19]. Benefitting from the structural flexibility, rationally designed MOFs with optimized transition metal centres and organic ligands can achieve enhanced chemical and electrochemical stability while maintaining high ionic conductivity, making them ideal candidates for artificial CEIs. Among various ligands, triazole-based frameworks demonstrate ideal stability in air, boiling water and acidic media[20]. For metal ions, Zn^{2+} proves to be an optimal choice for enhancing electrochemical stability[21]. Therefore, we selected MET-6 as the candidate MOF epilayer, a framework comprising Zn^{2+} and H-1,2,3-triazole.

The Na^+ diffusion pathway in the MET-6 tunnel was validated by $^1H-^{13}C$ heteronuclear correlation (HetCor) nuclear magnetic resonance (NMR) spectroscopy and ab initio molecular dynamics (AIMD) simulations. Typically, the PEO chains and sodium salts penetrate the MOFs' channel, establishing a Na^+ diffusion network[16]. To confirm the encapsulation of polymer chains within the pores, we used $^1H-^{13}C$ HetCor NMR spectroscopy, which detects magnetization transfer between spatially proximate species during contact time. As illustrated in Fig. 1c, the magnetization transfer between ^{13}C of PEO and ^1H of MET-6 marked by blue lines can be directly observed, meaning PEO chains penetrate the MOFs' channels. Furthermore, AIMD simulations were performed to illustrate the Na^+ ion-transport mechanism in the pore of MET-6. Figure 1d exhibits AIMD trajectory snapshots at $t = 10$ ps, revealing that Na^+ ions are solvated by both FSI^- and PEO, with bond lengths of ~2 Å corresponding to the first solvation shell. The mean square displacement (MSD) of Na^+ and FSI^- ions from AIMD trajectories is exhibited in Fig. 1e. It can be observed that Na^+ ions diffuse much faster than FSI^- anions due to the ion-sieving capability of MET-6 channels, resulting in a high Na^+ transference number.

The key point for realizing isotropic MOF epilayer is ensuring MOF connects with cathode surfaces, given the relatively low lattice deformation energy[19]. Therefore, the interaction between ligands and substrates is crucial[22]. MET-6 [$Zn(C_2N_3H_2)_2$] and ZIF-8 [$Zn(C_4N_2H_5)_2$] with different ligands [$C_2N_3H_2-H$ or $C_3N_2H_2-CH_3$] have been deliberately selected to clarify the epitaxial growth mechanism of MOFs on NVOPF surfaces (Supplementary Figs. 1–3 and Supplementary Tables 1 and 2). NVOPF was synthesized following previously reported methods (Supplementary Figs. 4 and 5). NVOPF can be indexed to the *I4/mmm* space group; therefore, the square surfaces are (001) planes (the top and bottom surfaces), while the rectangle shape surfaces are (100) planes (the side surfaces) (Fig. 2a,b). This phenomenon is further validated by the integrated phase-contrast scanning transmission electron microscopy (TEM) results (Supplementary Fig. 6). Through liquid-phase quasi-epitaxial growth, the ligands [$C_2N_3H_2-H$ or $C_3N_2H_2-CH_3$] and metal ion [$Zn(C_2H_3O_2)_2$] were dissolved in the NVOPF dispersion to establish the MOF epilayer. XRD patterns of MVOPF, NVOPF@MET and NVOPF@ZIF confirm the formation of MOFs (Supplementary Figs. 7–9 and Supplementary Tables 3–5). However, the epitaxial growth behaviours are obviously different (Fig. 2a). As shown in Fig. 2b and Supplementary Figs. 10–14, MET-6 forms relatively uniform epilayers across all exposed particle surfaces, while ZIF-8 selectively coats only the (001) planes. Based on the above findings, we can speculate that the crystal face selective growth behaviour of NVOPF@MET and NVOPF@ZIF might be dominated by the ligand–NVOPF surface interactions. This striking difference in growth behaviour prompted us to investigate the underlying mechanism.

To reveal this selectivity, first principal calculations were performed to quantify the absorption energies of ligands on the NVOPF surfaces (Supplementary Note 1). As shown in Fig. 2c and Supplementary Fig. 15a–d, the absorption energies of $C_2N_3H_3$ on the (001) and (100) planes are −0.51 eV and −0.58 eV, respectively. By contrast, for $C_3N_2H_2-CH_3$, they are −0.67 eV on the (001) plane, but merely −0.05 eV on the (100) plane, which is attributed to the electrostatic repulsion between the $-CH_3$ group and Na atoms. Therefore, the low absorption energy between the $C_3N_2H_2-CH_3$ and (100) plane leads to the crystal-face-selective growth of NVOPF@ZIF. Interestingly, the solvent and anion in the liquid phase reaction system should also be considered. We deliberately designed a series of synthesis strategies, confirming the connection between ligands and substrate is the key factor for designing an isotropic MOF epilayer (Supplementary Fig. 16a–c). Benefitting from the uniformity and stability (triazole-based framework), NVOPF@MET demonstrates notably better chemical and electrochemical performance (Supplementary Fig. 17).

Beyond achieving isotropy, controlling the epilayer's morphology presents another critical challenge. Suppressing Ostwald ripening is the key to obtaining uniform, thin epilayers. We used rapid nucleation to consume reactants early, generating small nuclei and preventing subsequent Ostwald ripening. Supplementary Fig. 18 shows how Ostwald ripening affects layer uniformity. Although rapid nucleation represents a straightforward approach to suppress Ostwald ripening, it introduces uniformity challenges, as indicated by the dispersed aggregated islands observed on epilayers (Supplementary Fig. 11). In principle, using more complex synthetic strategy, such as surfactants, sacrificial templates or other environment-modulating agents, to precisely control the MOF growth environment, can improve uniformity further[23].

Finally, spectroscopic and structural characterizations were conducted to confirm the relatively uniform MET-6 epilayer. As shown in Supplementary Figs. 9 and 19, the peak belonging to MET-6 can be clearly captured by X-ray diffraction (XRD) and Fourier transform infrared (FT-IR) patterns of NVOPF@MET. Moreover, the microstructures of NVOPF and NVOPF@MET are probed by cryo-TEM (Fig. 2d). Unlike NVOPF, a ~4-nm-thick amorphization layer is observed on the surface of NVOPF@MET particles, which can be attributed to the electron-beam-sensitive nature of MOFs (Supplementary Figs. 20 and 21). The corresponding energy-dispersive spectrometry (EDS) mapping images and X-ray photoelectron spectroscopy results confirm the co-existence and relative uniform distribution of Zn and C within the epitaxial coating layer (Fig. 2e and Supplementary Fig. 22). These results collectively demonstrate that our approach enables a facile room-temperature one-step synthesis strategy for building isotropic MOF epilayers on cathode surfaces.

Enhanced rate capability and cycling stability

The electrochemical performance of NVOPF and NVOPF@MET cathodes was evaluated using PEO-based solid-state Na batteries. Specifically, the batteries were assembled with as-prepared materials as the cathode, NaFSI-PEO as the electrolyte and metallic sodium as the anode. The NaFSI-PEO electrolyte was prepared following a previously reported method[24] and demonstrated prolonged cycling stability with a metallic sodium anode (Supplementary Fig. 23). First, NVOPF@MET with varying MET-6 contents (0–5 wt%, wt% = $m_{\text{MET-6 raw material}}/m_{\text{NVOPF}}$; m, mass) was synthesized for optimization (Supplementary Figs. 24 and 25). As shown in Supplementary Fig. 26, pristine NVOPF and a series of NVOPF@MET showed similar charge/discharge curves but different initial Coulombic efficiency, when charged/discharged at 0.1 C (with 1 C defined as 120 mA g^{-1}) between 2.5 V and 4.2 V versus Na^+/Na at 80 °C. The results demonstrate that the best composition is NVOPF with 4 wt% of MET-6 raw materials (NVOPF@MET-4wt), which increases the initial Coulombic efficiency from 84.07% to 93.33%. Moreover, the cycling performance of the as-prepared materials in Supplementary Fig. 27 corroborates this conclusion, with NVOPF@MET-4wt retaining 99.3% capacity after 50 cycles. Consequently, NVOPF@MET-4wt is denoted as NVOPF@MET for subsequent characterization.

We emphasize that using polyvinylidene fluoride (PVDF) as the binder is questionable when discussing the electrochemical stability of solid-state electrolytes with specific cathode surfaces, owing to its limited ion conductivity and obstructed connection between the electrolyte and cathode material. The electrochemical tests of pristine NVOPF and NVOPF@MET were performed with PVDF and

https://doi.org/10.1038/s41560-025-01857-y

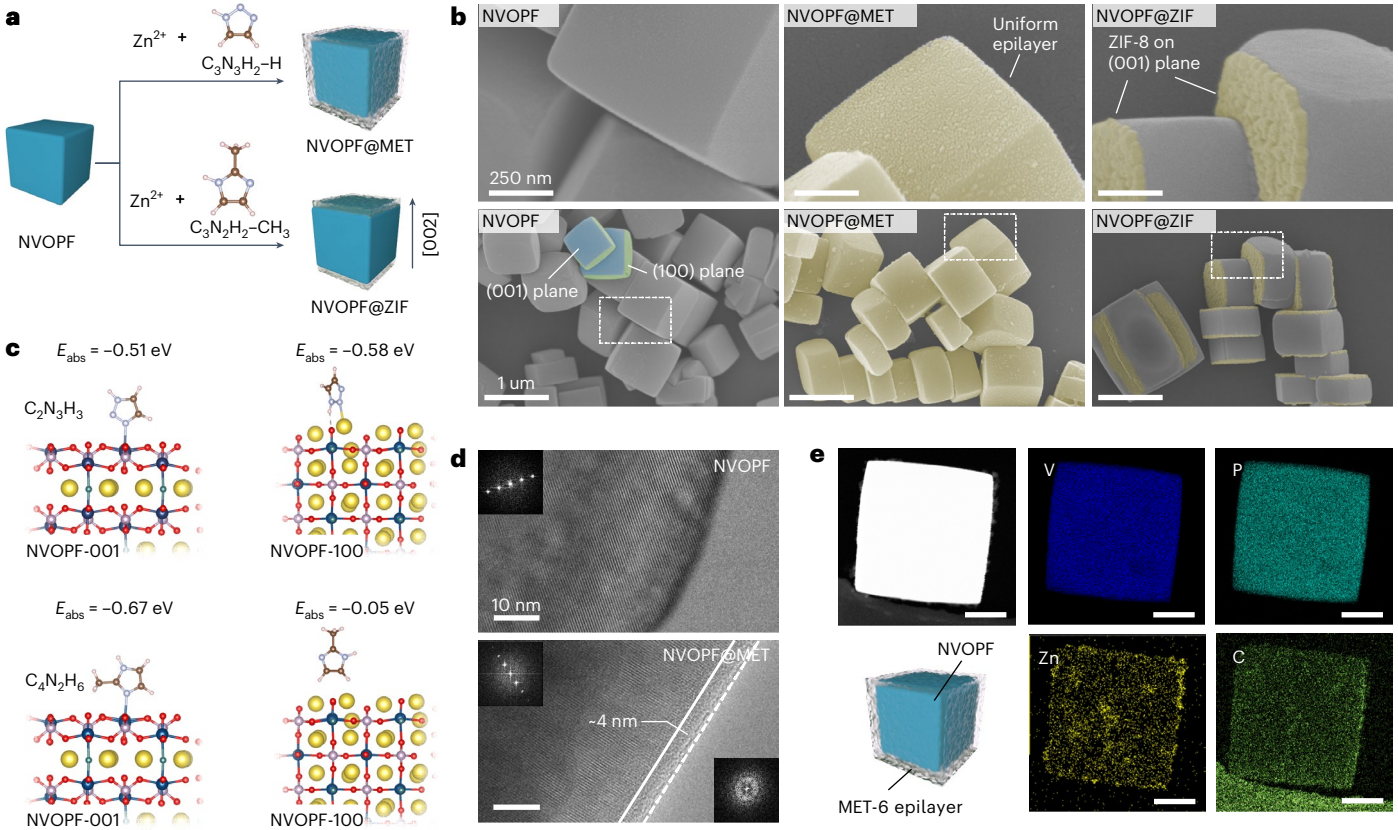

Fig. 2 | Characterization of the isotropic MOF epilayer. a, Schematic diagrams of the ZIF-8 and MET-6 self-assembly behaviours. **b**, SEM images of NVOPF, NVOPF@MET and NVOPF@ZIF, respectively. MET-6 is thoroughly coated on the NVOPF surface, but only the (001) plane can be coated by ZIF-8. **c**, DFT calculations of the absorption energy (E_{abs}) between ligand [$C_2N_3H_2$–H or $C_3N_2H_2$–CH_3] and crystal plane [(001) or (100)]. Na, yellow; V, blue; P, grey; F, cyan; O, red; C, brown; H, white. **d**, Cryo-TEM images of NVOPF and NVOPF@MET. Inset: the fast Fourier transformation (FFT) images of NVOPF diffraction fringes and electron-beam radiation-damaged amorphous MET-6. **e**, Elemental distributions (V, P, Zn and C) of the NVOPF@MET particle. Scale bar, 300 nm.

PEO binders, respectively (denoted as NVOPF-PVDF, NVOPF-PEO, NVOPF@MET-PVDF and NVOPF@MET-PEO). Notably, the voltage profile of NVOPF-PEO exhibits a continuous side reaction during charging, whereas this phenomenon is absent in the NVOPF-PVDF voltage profile (Fig. 3a and Supplementary Fig. 26). By contrast, NVOPF@MET-PEO delivers excellent electrochemical stability, indicating its inherent high-voltage stability (Fig. 3b). Moreover, NVOPF@MET-PEO exhibits improved rate capability at various discharge current densities of 0.2 C, 0.3 C, 0.5 C, 1 C, 2 C and 5 C (with 1 C defined as 120 mA g^{-1}), retaining 93.3% of its capacity at 2 C relative to 0.2 C (Fig. 3c–e).

Long-term cycling highlighted the MET-6 epilayer's stability. Figure 3f and Supplementary Fig. 28 show the cycling performance of NVOPF-PVDF, NVOPF@MET-PVDF and NVOPF@MET-PEO at 0.5 C. For NVOPF-PVDF, the Coulombic efficiency experienced a sudden collapse, retaining only 78.6% of the initial capacity after 130 cycles, accompanied by obvious voltage polarization (Supplementary Fig. 29). By contrast, NVOPF@MET exhibited excellent stability with high capacity retention. The stability of the MET-6 epilayer was further verified through XRD and EDS mapping. The XRD patterns of cycled NVOPF@MET retained the characteristic Bragg positions of MET-6 (Supplementary Figs. 9 and 30), while EDS mapping revealed largely uniform distributions of Zn, N and C elements (Fig. 2e and Supplementary Fig. 31), confirming that the MET-6 epilayer remained intact during cycling. Similar to ether electrolytes, the interface between metallic sodium and PEO electrolytes maintained a relatively flat morphology during deposition/stripping cycles (Supplementary Fig. 32). These promising results motivated extended cycling tests, which revealed an impressive cycling lifetime of 1,500 cycles with 77.9% capacity retention at 2 C for NVOPF@MET-PEO (Fig. 3g). As shown in Supplementary Fig. 33 and Supplementary Table 6, an extensive comparison with previously published findings demonstrates the advantage of the MET-6 epilayer in delivering long-term stability for high-voltage PEO-based all-solid-state cells.

To evaluate commercial potential, pouch cells were fabricated using NVOPF@MET as the cathode, NaFSI-PEO as the electrolyte and sodium metal as the anode. The cells were assembled under minimal pressure (5.2 kPa, close to ambient pressure) to optimize initial interfacial contact. As shown in Fig. 3h, the pouch cell delivers excellent cycling performance, maintaining 80% of the initial capacity after 300 cycles at a current density of 0.5 C within a voltage window of 2.5–4.2 V. Furthermore, the cells exhibited excellent voltage stability, retaining 97.9% of the average discharge voltage with only a 0.07 V decrease (Supplementary Fig. 34), underscoring their practical viability.

Failure analysis of the PEO at high voltage

The high reversibility of NVOPF@MET indicates that the interfaces between cathodes and electrolytes play a dominant role in high-voltage stability, which can mitigate continuous side reactions between the cathode and electrolyte under high-voltage conditions. Typically, the LSV technique has been widely used to assess the electrochemical stability of electrolytes, wherein the electrolyte is sandwiched between stainless-steel sheets. However, the reliability of conventional LSV results is limited, as the electrolyte's operating voltage varies across different cathode materials[25,26]. To address this limitation, we developed a high-sensitivity LSV–GCMS characterization method (Detailed in Fig. 4a and Supplementary Note 2). This approach enables precise

https://doi.org/10.1038/s41560-025-01857-y

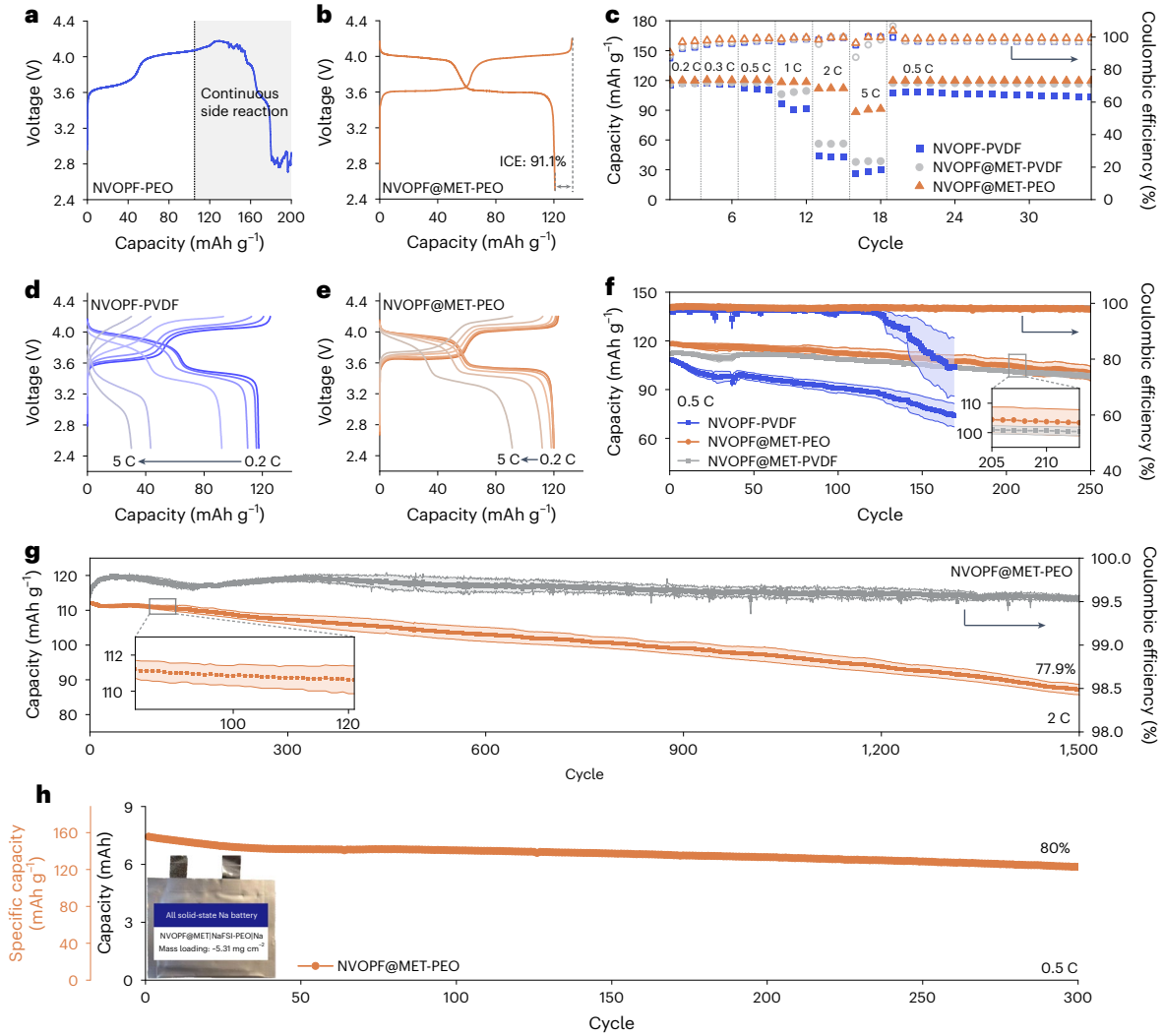

Fig. 3 | Electrochemical performances of ASSBs with as-prepared materials. **a**,**b**, The voltage profiles of NVOPF (**a**) and NVOPF@MET (**b**) with PEO binder (denoted by NVOPF-PEO and NVOPF@MET-PEO) at 0.1 C. ICE, initial Coulombic efficiency. **c**–**e**, Rate performance of NVOPF-PVDF (**c**), NVOPF@MET-PVDF (**d**) and NVOPF@MET-PEO (**e**). **f**, Cycling performance of the ASSBs with NVOPF-PVDF, NVOPF@MET-PVDF and NVOPF@MET-PEO cathodes at a current density of 0.5 C. **g**, Long-term cycling performance of NVOPF@MET-PEO ASSB at 2 C. **h**, Cycling performance of the all-solid-state Na battery pouch cell with NVOPF@MET-PEO cathodes (~5.31 mg cm^{-2}). Test temperature, 80 °C. Data are presented as mean values ± s.e.m., and the sample number is 3. (1 C = 120 mA g^{-1}).

quantitative and qualitative analysis of released gases during electrochemical reactions. Consequently, it can accurately determine the electrolyte's oxidation potential when in contact with specific cathode materials. Furthermore, the detailed gas information provides valuable insights into revealing the oxidation pathways of the electrolyte. Although LSV–GCMS provides high sensitivity for detecting gas evolution, its detection interval (~3.7 min per chromatogram) inevitably averages out events occurring on timescales shorter than a few minutes. To reconcile this, we used a slow LSV scan rate of 0.02 μV s^{-1}. Consequently, the method provides operando, minute-scale resolution adequate for the gradual electrolyte oxidation studied here; subminute transients would require faster detectors such as direct-inlet mass spectrometry (Supplementary Fig. 35).

The LSV–GCMS data (Fig. 4b,c) present integrated LSV profiles (black curves, bottom) and corresponding GCMS results (coloured curves, top). For bare NVOPF surfaces, aggressive PEO decomposition initiates at 3.87 V (Fig. 4b). Interestingly, although the PEO monomer is C_2H_4O belongs to the C_{2+} species, the predominant organic component in GCMS is C_3H_6 (a C_{3+} species). Meanwhile, the CO_2 curve is perfectly consistent with that of C_3H_6. Based on the aforementioned experimental results and previous accumulations on PEO's oxidation pathway, it can be attributed to the breakage of C–O bonds along the PEO backbone under high-voltage conditions (Supplementary Note 3 and Supplementary Figs. 36 and 37). Notably, cathode surface catalytic activity, particularly at transition metal sites, directly influences the PEO decomposition process[25,27]. Beyond the high electrode potential at the cathode surface, a more critical factor triggering premature decomposition is the reduced intrinsic stability of PEO upon direct cathode contact. This understanding has led to the widespread adoption of surface coating strategies to prevent direct PEO–cathode contact. Here, unlike traditional coating materials, MET-6 offers distinct advantages. When PEO molecules penetrate the MOF pores, they not only retain efficient ionic transport but also exhibit enhanced stability within the confined channels, attributed to the spatial confinement effect[28] (Fig. 1c–e). Consequently, MOF epilayers serve dual functions: providing favourable electrochemical stability while enabling enhanced rate performance through their distinctive structural characteristics. As shown in Fig. 4c, the oxidation potential of PEO can be extended to 4.27 V after taking the MET-6 epilayer. These findings not only validate LSV–GCMS as a powerful characterization tool for probing the electrolyte's operating window, but also substantiate the good electrochemical performance of the MOF epilayer as a rationally designed artificial CEI.

https://doi.org/10.1038/s41560-025-01857-y

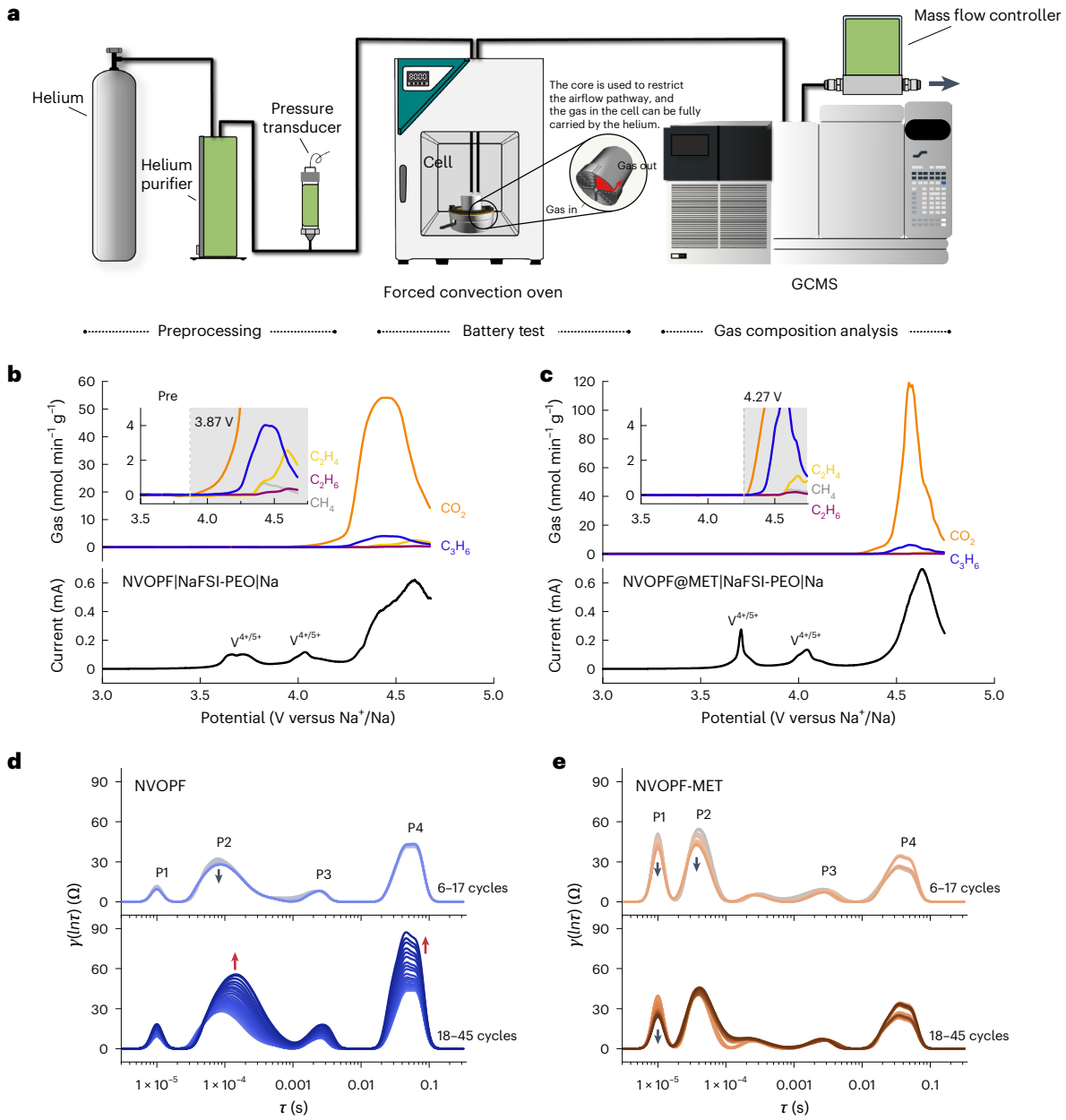

Fig. 4 | The degradation mechanism of the PEO electrolyte. a, An illustration of the LSV–GCMS technique. **b**, LSV–GCMS of a cell using an NVOPF-PEO cathode. **c**, The same measurement using an NVOPF@MET-PEO cathode. In both panels, the black curve is the LSV trace and the coloured curves are gas compositions versus voltage. **d**,**e**, DRT profiles of NVOPF-PEO (**d**) and NVOPF@MET-PEO (**e**), respectively. The EIS characterization is conducted after each cycling, and the current density is 0.2 C (1 C = 120 mA g^{-1}).

To clarify the mechanism, we performed DFT calculations. The charged NVOPF surface is highly catalytic: when electrolytes adsorb, the C–O bonds are markedly weakened, with the integrated crystal-orbital Hamilton population (–ICOHP) decreasing from 8.8 eV to 6.2 eV, and hydrogen abstraction occurring on the reactive (100) facet (Supplementary Fig. 38a,b). Notably, these are similar locations that serve as anchoring points for the MET-6 epilayer. This finding implies that the formation of the epilayer selectively passivates the high-reactive regions of the cathode surface (Fig. 2c). Furthermore, spatial freedom is a prerequisite for molecules to adopt energetically favourable conformations for low-voltage decomposition, and the MET-6 nanopores effectively curtail this reactivity. As illustrated in Supplementary Fig. 38c,d, the –ICOHP of the C–O bond is highly dependent on the molecule's orientation. The nanoporous architecture of MET-6 physically restricts PEO segments from achieving this most reactive conformation. The above findings provide a theoretical basis for the enhanced electrolyte stability conferred by the MET-6 epilayer.

In situ electrochemical impedance spectroscopy (EIS) further illustrates interfacial evolution dynamics. Nyquist profiles collected from 1–45 cycles are shown in Supplementary Fig. 39, where NVOPF is presented on the left and NVOPF@MET is on the right. The overall cell resistance of NVOPF continuously shifts to higher values, indicative of the hindered Na^+ diffusion pathway. By contrast, NVOPF@MET maintains consistent impedance characteristics throughout the cycling process. The distribution of relaxation times (DRT) method is further used to analyse the frequency-based EIS spectrum[29–31] (Supplementary Note 4). According to previously reported results, the four impedance peaks in Fig. 4d,e (P1, P2, P3 and P4) can be attributed to the resistive interface/space charge layer, solid electrolyte interface layer, charge transfer and diffusion, respectively[32–35] (Supplementary Note 4).

The interface/space charge layer (P1) in NVOPF@MET is 51.3 Ω after six cycles, higher than NVOPF (12.1 Ω). However, interestingly, the peak value of P1 in NVOPF@MET decreases to 23.9 Ω after 45 cycles, which means the resistance of the MET-6 epilayer is reduced after cycling. This occurs because both NaFSI salt and PEO chains penetrate the MOF pores during cycling, establishing efficient Na^+ diffusion pathways (Fig. 1c–e and Supplementary Fig. 40). Therefore, although the MET-6 epilayer initially contributes to higher resistance, this resistance decreases obviously with continued cycling. P2 peak is attributed to the solid electrolyte interlayer. Continuous interfacial side reactions can cause by-products to accumulate on the cathode surface, leading to interfacial resistance continuously increasing. Therefore, the P2 peak can be a probe for the electrochemical stability of the CEI. Notably, NVOPF shows a rapidly increased resistance after 17 cycles (from 29.4 Ω to 59.7 Ω), which reveals a continuous side reaction on the cathode surface. In addition, the P2 peak of NVOPF gradually shifts towards lower frequencies as cycling progresses, consistent with continuous CEI growth. The thickening interphase increases resistance and extends the ion diffusion path, thereby increasing the time constant (τ). P4 reflects the diffusion impedance of the cathode particles. Interfacial side reactions deteriorate the ion- and electron-transport pathways, gradually isolating NVOPF particles. This network degradation raises the diffusion impedance substantially, while the characteristic time constant τ remains almost unchanged (Fig. 4d). By contrast, the peak values of P2–4 stay unchanged for NVOPF@MET, confirming the favourable electrochemical stability of the MET-6 epilayer (Fig. 4e).

These comprehensive analyses demonstrate that aggressive PEO decomposition on bare NVOPF surfaces at high voltages leads to substantial interfacial resistance, voltage polarization and capacity degradation. Moreover, they validate the enhanced electrochemical performance of the MET-6 epilayer as a stable, robust, uniform MOF-based architecture featuring efficient Na^+ ion diffusion channels.

Outlook of isotropic MOF epilayer beyond solid-state batteries

Surface engineering is an effective strategy for addressing interface issues between cathodes and electrolytes, such as the dissolution of transition metal ions and particle pulverization. While epitaxial growth is regarded as an effective strategy for realizing ideal coating layers, the anisotropic nature of crystal facets offers a formidable obstacle, restricting uniform epitaxial growth to the entire cathode surface. MOFs are poised to become the paradigm for achieving isotropic epilayers, due to their low distortion energy and flexible skeletal structures. In addition, excellent ionic conductivity and chemical and electrochemical stability can be realized by adjusting MOF structures, indicating the potential for addressing interfacial issues.

Beyond solid-state systems, we also achieved an isotropic MET-6 epilayer on the $Na_2Mn[Fe(CN)_6]\cdot H_2O$ (PW) as the aqueous battery cathode to validate the isotropic MOF epilayer's high applicability and universality (Supplementary Figs. 41 and 42). The aqueous Na-ion batteries are assembled with PW (or PW@MET) as the cathode, active carbon as the anode and 17 M $NaClO_4$ as the electrolyte. Benefitting from the chemical and electrochemical stability of the MET-6 epilayer, the dissolution of transition metals such as Fe/Mn for the Prussian white cathode was diminished (Supplementary Note 5). As a result, PW@MET demonstrates long-term stability at room temperature, lasting up to 1,000 h and retaining 80% of its initial capacity after 800 cycles at a current density of 200 mA g^{-1} (Supplementary Figs. 43 and 44). In addition, the Coulombic efficiency of PW@MET is as high as ~98%.

In summary, we propose a powerful strategy for achieving isotropic epitaxial growth on cathode surfaces. Specifically, a relative uniform and dense isotropic MOF epilayer can be self-assembled on the $Na_3V_2O_2(PO_4)_2F$ surfaces at room temperature by adjusting the ligand's surface adsorption energies. Benefitting from their excellent electrochemical stability and robust interfacial connection, the PEO electrolyte exhibited a long cycling lifetime at a high cut-off voltage of 4.2 V, maintaining up to 80% of the initial capacity after 1,500 cycles. In addition, the universality of the isotropic MOF epilayer is confirmed beyond solid-state batteries, indicating the rationally designed epilayer offers a guideline for sophisticated CEI engineering. Interestingly, the structural diversity and tunability of MOFs, facilitated by the judicious selection of ligand and metal ion species, offer opportunities for tailoring the epilayer composition to specific cathode surfaces or enabling functional applications.

Methods

Preparation of $Na_3V_2O_2(PO_4)_2F$ (NVOPF)

NVOPF is synthesized by the previously reported co-precipitation method[36,37]. $VOSO_4\cdot xH_2O$ (99.9%, Alfa), NaH_2PO_4 (96%, Alfa) and NaF (99%, Acros) were added and dissolved in deionized water (the molar ratio of V:P:F is 1:3:1.7). The pH value was adjusted to 6 by $NH_3\cdot H_2O$. After several days, the powder of NVOPF was washed with deionized water and dried in the oven at 120 °C for 6 h.

Preparation of $Zn(C_2N_3H_2)_2$ (MET-6)

A total of 1.62 g (7.34 mmol) of $Zn(CH_3COO)_2\cdot 2H_2O$ (97%, Alfa) was dissolved in 40 ml solvent mixture (*N*,*N*-dimethylformamide (DMF):ethanol:water:$NH_3\cdot H_2O$ (30%) = 2:2:3:1). Subsequently, 1.25 ml (21.6 mmol) of 1H-1,2,3-triazole (98%, Tokyo Chemical Industry (TCI)) was added dropwise to the above solution and stirred for 30 min. The powder was washed with DMF and methanol several times and immersed in methanol for 3 days, exchanging the solvent three times. Finally, the solvent was removed by vacuum oven for 24 h at 60 °C (ref. 38).

Preparation of $Zn(C_4N_2H_5)_2$ (ZIF-8)

A total of 2.20 g (10 mmol) of $Zn(CH_3COO)_2\cdot 2H_2O$ was dissolved in 200 ml methanol (denoted as solution A), and 6.57 g (80 mmol) of 2-methylimidazole (97%, Alfa) was dissolved in 200 ml methanol (denoted as solution B). Solution A was rapidly poured into B with vigorous stirring for 1 h. The powder was washed with methanol several times. Finally, the solvent was removed by vacuum oven for 24 h at 60 °C (ref. 39).

Preparation of NVOPF@MET

A total of 0.087 g (4 wt%, based on the raw material) of $Zn(CH_3COO)_2\cdot 2H_2O$ was dissolved in 14 ml solvent mixture (DMF:ethanol:water = 2:2:3). $NH_3\cdot H_2O$ was added dropwise until the precipitation disappeared under stirring, after which 2 g of NVOPF was dispersed in the solution. Subsequently, 100 µl of 1H-1,2,3-triazole was added dropwise to the above solution and stirred for 30 min. The powder was washed with water and ethanol several times, and the solvent was removed by vacuum oven for 24 h at 60 °C. Other mass ratios have been synthesized with the same method.

Preparation of NVOPF@ZIF

A total of 0.154 g (8 wt%, yield accounted for) of $Zn(CH_3COO)_2\cdot 2H_2O$ was dissolved in 10 ml methanol (denoted as solution A), and 6.57 g (80 mmol) of 2-methylimidazole was dissolved in 200 ml methanol, after which 2 g of NVOPF was dispersed in the solution (denoted by solution B). Solution A was rapidly poured into B with vigorous stirring for 1 h. The powder was washed with ethanol several times. Finally, the solvent was removed by vacuum oven for 24 h at 60 °C.

Preparation of PW@MET

$Na_2Mn[Fe(CN)_6]\cdot H_2O$ (denoted by PW) was synthesized by a ball milling method[40]. Specifically, 0.735 g (3 mmol) of $Mn(CH_3COO)_2\cdot 4H_2O$ and 1.452 g (3 mmol) of $Na_4Fe(CN)_6\cdot 10H_2O$ were ball milled at 900 rpm for 1.5 h. The powder was washed with deionized water and ethanol, and

dried in a vacuum oven at 120 °C for 24 h. For PW@MET, the synthesis method was similar to that of NVOPF@MET.

PEO-based solid-state electrolyte

A total of 1.152 g of sodium bis(fluorosulfonyl)imide (NaFSI) was dissolved in 80 ml water, after which 0.061 g of Al_2O_3 (γ phase, 10 nm, Aladdin) was dispersed in the solution. Five grams of PEO (M.W. 600,000, Acros) was added in the above solution, with stirring at 60 °C for 24 h. The resulting viscous solution was then cast onto a Teflon plate, and the solvent was evaporated slowly at 35 °C. Furthermore, the solvent was thoroughly removed by vacuum oven at 60 °C for 12 h (ref. 24).

Electrochemical characterization

The active material was mixed with conductive additive (Super P) and binder (80:10:10 ratios) to form a slurry that was coated onto aluminium foil. For the PVDF (Solef5130, Solvay) binder, *N*-methylpyrrolidone was used as solvent, and the coated aluminium foil was dried in the vacuum oven at 120 °C for 12 h. The PEO binder was fabricated with a similar method, detailed in the electrolyte synthesis process; the coated aluminium foil was predried at room temperature for 12 h, and further transferred to the vacuum oven at 120 °C for 12 h. Then, the coated foil was punched into discs with a diameter of 10 mm (~2.0 mg cm^{-2}). The 2032 coin-type cells were assembled in an Ar atmosphere glove box with a cathode, an anode of metallic Na (99.8%, Alfa) and a PEO-based solid-state electrolyte. The coin cells were placed in forced convection at 80 °C, and the LAND CT3200A battery cycler was performed for the electrochemical characterization.

Fabrication of the pouch cell

The all-solid-state Na-ion batteries pouch cell was assembled with NVOPF@MET-PEO as a cathode, PEO-based electrolyte and metallic Na as an anode. The cathode area was 12 cm^2 (4 cm × 3 cm), and the load mass was ~5.31 mg cm^{-2}. The PEO-based solid-state electrolyte was cut into 4.5 cm × 3.5 cm. The sodium ingot (99.8% Alfa) was rolled into sodium foil. For the anode, the 300-μm-thick nickel foam was rolled and cut into 4.25 cm× 3.25 cm (12 μm after rolling), the sodium foil was rolled on the rolled nickel foam and the excess sodium foil was cut off. The pouch cells were assembled and sealed in a laminated aluminium film bag. The cycling performance of the pouch cell was determined on a LAND CT3200A within 2.5-4.2 V (versus Na^+/Na) at 80 °C under 5.2 kPa.

Materials characterization

XRD was conducted using a Bruker D8 Advance diffractometer (Cu Kα radiation source, λ Kα1 = 1.54056 Å, λ Kα2 = 1.54439 Å) over a 2θ range of 5–80°. GSAS2 was performed to calculate the Rietveld refinement profile. FT-IR (Bruker VERTEX 70 V) was used to capture the functional group. X-ray photoelectron spectroscopy of Zn 2*p* and N 1*s* were collected by Thermo Fisher ESCALAB 250 Xi (Thermo Fisher with monochromatic 150 W Al Kα radiation). STA 449 F1 Jupiter carried out the thermogravimetric analysis characterization with mixed gas ($Ar:O_2$ = 5:1, volume ratio) at a heating rate of 10 °C min^{-1}. N_2 gas absorption isotherm analysis was performed on a NOVA 2000e porosimetry analyser, and the measurement was conducted at 77 K on activated samples of MET-6 before and after NaFSI impregnation. The resolution of the X-ray tomography was 200 nm. The CTAn and CTVox software were used for the analysis and image rendering.

Electron microscopy

The morphology of the cathode particle was observed by scanning electron microscopy (SEM; S-4800, Hitachi) with acceleration voltages of 10 kV. For the cross-sectional morphology analysis of the cells after cycling, copper and aluminium foils were cut into discs with a diameter of 16.2 mm and assembled into the coin cells in the following sequence: copper foil, metallic Na, PEO electrolyte, cathode and aluminium foil. This arrangement allows easy separation of the electrode with the PEO electrolyte from the stainless-steel case. The coin cells were immersed in the liquid nitrogen for 1 h and rapidly transferred to the Ar atmosphere glove box for disassembling. Finally, the electrode with PEO electrolyte was cut, and a clear section was obtained. Cryo-(S)TEM characterizations were carried out using a JEOL JEM ARM200F microscope under cryogenic temperatures (−180 °C) at 200 kV. The grid was loaded on the cryo-TEM holder (Fischione 2550) equipped with a tip retraction device. Liquid nitrogen was added to the cryo-TEM holder, and the sample temperature dropped and stabilized at −180 °C. To minimize the beam damage to the sample, we usually started with an ultralow dose, then gradually increased the dose to improve the signal-to-noise ratio of the image without damaging the sample. The integrated phase-contrast scanning TEM imaging was conducted in a Cs-corrected STEM (FEI Titan Cubed Themis G2 300) operated at 300 kV. The STEM is equipped with a DCOR+ spherical aberration corrector for the electron probe, which was aligned with proper aberration coefficients using a standard gold sample.The obtained images were processed using a low-pass Gaussian filter for denoising and smoothing.

EIS measurements

EIS measurements were performed with a Zahner IM6 electrochemical workstation for the NVOPF-PVDF and NVOPFM@MET-PVDF cells. The battery cycling module was used due to the fully automatic in situ measurement program. The galvanostatic charge/discharge was conducted with a current density of 0.2 C (1 C = 120 mA g^{-1}) within the voltage range of 2.5–4.2 V (versus Na^+/Na) at 80 °C. An applied a.c. potential of 5 mV over a frequency range from 1 MHz to 1 Hz was used for the EIS measurement. The EIS measurements of every cycle were conducted after 1 h for relaxation.

LSV–GCMS technique

The oxidation potential of the electrolyte is varied when connected to different cathode surfaces. Typically, the LSV technique has been introduced to characterize the oxidation potential of the solid-state electrolyte, where the electrolyte is sandwiched between two stainless-steel sheets. However, the result often deviates substantially from the actual oxidation potential of assembled batteries—for example, LSV may show an oxidation potential as high as 4.8 V, yet noticeable capacity fading occurs during cycling at a 4.2 V cut-off. In this work, a self-built LSV–GCMS system combining linear sweep voltammetry (LSV, CHI 660e, Shanghai Chenhua Instrument), gas chromatography and mass spectrometry (Agilent 5977C GC/MSD) was developed and used to highlight the importance of CEI design principles.

During preprocessing, the helium was purified by heated helium purifiers (HP2-220, VICI), and the pressure was detected and controlled to 2 atm (Omega PX409). A high-accuracy mass flow controller (CS100, Beijing Sevenstar Flow) was installed at the outlet, maintaining a flow rate of 4 μl min^{-1}. In the cell, the core was designed to restrict the airflow pathway, so the generated gas can be fully carried by the helium. In addition, a mini forced convection oven was used to maintain a test temperature of 80 °C. Finally, 2.5 ml gas was captured by GCMS for gas composition analysis.

Two-dimensional HetCor NMR

Solid-state NMR experiments were conducted on a Bruker Neo 600 MHz spectrometer. HetCor spectra were measured at 12.0 kHz magic-angle spinning (MAS) with frequency-switched Lee–Goldburg homonuclear decoupling, 1,000 μs of contact time, 0.3 ms of cross-polarization and total suppression of sidebands (TOSS) before detection.

Simulations

Density functional theory (DFT) calculations of the adsorption energy were performed using spin-polarized methods within the plane-wave DFT framework, employing the Vienna Ab initio Simulation Package (VASP)[41–43] using the generalized gradient approximation of

Perdew–Burke–Ernzerhof to calculate the total energies[44]. A cut-off energy of 500 eV was used for all calculations. The force exerted on each atom was ensured to be less than 0.02 eV $Å^{-1}$ for structural relaxation. The Brillouin zone was sampled by a $2 \times 2 \times 1$ Γ-centred k-mesh.

For AIMD simulations, the initial structure was built by randomly placing 2NaFSI + 2PEO [HO–$(CH_2O)_{15}$–H] in the pores of MOFs ($a = b = c = 17.665$ Å; $\alpha = \beta = \gamma = 90°$, the lattice parameters were collected by the XRD refinement profile). The AIMD simulations were carried out on a $1 \times 1 \times 1$ supercell at temperature of 80 °C, running for 13,000 steps with a time step of 1 fs. The first 3 fs were used to equilibrate the system at the temperature, and the MSD was calculated from the last 10 ps. Throughout the simulation, the H atoms within MOFs were allowed to adjust in response to the mobility of NaFSI and PEO.

Data availability

The data supporting the findings of this study are available within the Article and its Supplementary Information.

References

1. Armand, M. & Tarascon, J. M. Building better batteries. *Nature* **451**, 652–657 (2008).
2. Hu, Y.-S. Batteries: getting solid. *Nat. Energy* **1**, 16042 (2016).
3. Wu, E. A. et al. A stable cathode-solid electrolyte composite for high-voltage, long-cycle-life solid-state sodium-ion batteries. *Nat. Commun.* **12**, 1256 (2021).
4. Lee, M. J. et al. Elastomeric electrolytes for high-energy solid-state lithium batteries. *Nature* **601**, 217–222 (2022).
5. Cabañero Martínez, M. A. et al. Are polymer-based electrolytes ready for high-voltage lithium battery applications? An overview of degradation mechanisms and battery performance. *Adv. Energy Mater.* **12**, 2201264 (2022).
6. Seidl, L., Grissa, R., Zhang, L., Trabesinger, S. & Battaglia, C. Unraveling the voltage-dependent oxidation mechanisms of poly(ethylene oxide)-based solid electrolytes for solid-state batteries. *Adv. Mater. Interfaces* **9**, 2100704 (2021).
7. Yang, X. et al. Determining the limiting factor of the electrochemical stability window for PEO-based solid polymer electrolytes: main chain or terminal -OH group? *Energy Environ. Sci.* **13**, 1318–1325 (2020).
8. Goodenough, J. B. & Park, K. S. The Li-ion rechargeable battery: a perspective. *J. Am. Chem. Soc.* **135**, 1167–1176 (2013).
9. You, Y. & Manthiram, A. Progress in high-voltage cathode materials for rechargeable sodium-ion batteries. *Adv. Energy Mater.* **8**, 1701785 (2017).
10. Yoon, M. et al. Reactive boride infusion stabilizes Ni-rich cathodes for lithium-ion batteries. *Nat. Energy* **6**, 362–371 (2021).
11. Qiu, J. et al. Enabling stable cycling of 4.2 V high-voltage all-solid-state batteries with PEO-based solid electrolyte. *Adv. Funct. Mater.* **30**, 1909392 (2020).
12. Miyashiro, H. et al. Fabrication of all-solid-state lithium polymer secondary batteries using Al_2O_3-coated $LiCoO_2$. *Chem. Mater.* **17**, 5603–5605 (2005).
13. Zhu, X. et al. Epitaxial growth of an atom-thin layer on a $LiNi_{0.5}Mn_{1.5}O_4$ cathode for stable Li-ion battery cycling. *Nat. Commun.* **13**, 1565 (2022).
14. Tan, C., Chen, J., Wu, X.-J. & Zhang, H. Epitaxial growth of hybrid nanostructures. *Nat. Rev. Mater.* **3**, 17089 (2018).
15. Falcaro, P. et al. Centimetre-scale micropore alignment in oriented polycrystalline metal–organic framework films via heteroepitaxial growth. *Nat. Mater.* **16**, 342–348 (2017).
16. Zhao, R. et al. Metal–organic frameworks for solid-state electrolytes. *Energy Environ. Sci.* **13**, 2386–2403 (2020).
17. Wang, Z. et al. A metal–organic-framework-based electrolyte with nanowetted interfaces for high-energy-density solid-state lithium battery. *Adv. Mater.* **30**, 1704436 (2018).
18. Xu, W. et al. A metal–organic framework of organic vertices and polyoxometalate linkers as a solid-state electrolyte. *J. Am. Chem. Soc.* **141**, 17522–17526 (2019).
19. Wang, Z. et al. Nanoporous designer solids with huge lattice constant gradients: multiheteroepitaxy of metal–organic frameworks. *Nano Lett.* **14**, 1526–1529 (2014).
20. Suh, M. P., Park, H. J., Prasad, T. K. & Lim, D.-W. Hydrogen storage in metal–organic frameworks. *Chem. Rev.* **112**, 782–835 (2011).
21. Dong, P. et al. Toward high-performance metal–organic-framework-based quasi-solid-state electrolytes: tunable structures and electrochemical properties. *Adv. Mater.* **35**, e2211841 (2023).
22. Bristow, J. K., Butler, K. T., Svane, K. L., Gale, J. D. & Walsh, A. Chemical bonding at the metal–organic framework/metal oxide interface: simulated epitaxial growth of MOF-5 on rutile TiO_2. *J. Mater. Chem. A* **5**, 6226–6232 (2017).
23. Li, W., Zhu, Z., Chen, Q., Li, J. & Tu, M. Device fabrication and sensing mechanism in metal–organic framework-based chemical sensors. *Cell Rep. Phys. Sci.* **4**, 101679 (2023).
24. Liu, L. et al. In situ formation of a stable interface in solid-state batteries. *ACS Energy Lett.* **4**, 1650–1657 (2019).
25. Nie, K. et al. Increasing poly(ethylene oxide) stability to 4.5 V by surface coating of the cathode. *ACS Energy Lett.* **5**, 826–832 (2020).
26. Xu, S. et al. Ab initio modeling of electrolyte molecule ethylene carbonate decomposition reaction on $Li(Ni,Mn,Co)O_2$ cathode surface. *ACS Appl. Mater. Interfaces* **9**, 20545–20553 (2017).
27. Sun, G., Gao, J., Li, H. & Chen, L. Oxidized kinetic normal distribution models for sophisticated electrochemical windows. *J. Phys. Chem. C* **127**, 9554–9561 (2023).
28. Chang, Z. et al. A liquid electrolyte with de-solvated lithium ions for lithium-metal battery. *Joule* **4**, 1776–1789 (2020).
29. Lu, Y., Zhao, C.-Z., Huang, J.-Q. & Zhang, Q. The timescale identification decoupling complicated kinetic processes in lithium batteries. *Joule* **6**, 1172–1198 (2022).
30. Wan, T. H., Saccoccio, M., Chen, C. & Ciucci, F. Influence of the discretization methods on the distribution of relaxation times deconvolution: implementing radial basis functions with DRTtools. *Electrochim. Acta* **184**, 483–499 (2015).
31. Maradesa, A. et al. Advancing electrochemical impedance analysis through innovations in the distribution of relaxation times method. *Joule* **8**, 1958–1981 (2024).
32. Derakhshan, M., Sahraei, E. & Soudbakhsh, D. Detecting mechanical indentation from the time constants of Li-ion batteries. *Cell Rep. Phys. Sci.* **3**, 101102 (2022).
33. Pan, K., Zou, F., Canova, M., Zhu, Y. & Kim, J.-H. Comprehensive electrochemical impedance spectroscopy study of Si-based anodes using distribution of relaxation times analysis. *J. Power Sources* **479**, 229083 (2020).
34. Sun, S. et al. Eliminating interfacial O-involving degradation in Li-rich Mn-based cathodes for all-solid-state lithium batteries. *Sci. Adv.* **8**, eadd5189 (2022).
35. Zhang, R., Kondrakov, A., Janek, J. & Brezesinski, T. Timescale identification of electrochemical processes in all-solid-state batteries using an advanced three-electrode cell setup. *Energy Storage Mater.* **75**, 104000 (2025).
36. Qi, Y. et al. Scalable room-temperature synthesis of multi-shelled $Na_3(VOPO_4)_2F$ microsphere cathodes. *Joule* **2**, 2348–2363 (2018).
37. Zhang Q., et al. Large scale one-pot synthesis of monodispersed $Na_3(VOPO_4)_2F$ cathode for Na-ion batteries. *Energy Mater. Adv.* https://doi.org/10.34133/2022/9828020 (2022).

38. Gandara, F. et al. Porous, conductive metal-triazolates and their structural elucidation by the charge-flipping method. *Chemistry* **18**, 10595–10601 (2012).
39. Cravillon, J. et al. Rapid room-temperature synthesis and characterization of nanocrystals of a prototypical zeolitic imidazolate framework. *Chem. Mater.* **21**, 1410–1412 (2009).
40. He, S. et al. Solvent-free mechanochemical synthesis of Na-rich Prussian white cathodes for high-performance Na-ion batteries. *Chem. Eng. J.* **428**, 131083 (2022).
41. Kresse, G. & Furthmüller, J. Efficiency of ab-initio total energy calculations for metals and semiconductors using a plane-wave basis set. *Comput. Mater. Sci.* **6**, 15–50 (1996).
42. Kresse, G. & Furthmuller, J. Efficient iterative schemes for ab initio total-energy calculations using a plane-wave basis set. *Phys. Rev. B* **54**, 11169–11186 (1996).
43. Shi, S. et al. Multi-scale computation methods: their applications in lithium-ion battery research and development. *Chin. Phys. B* **25**, 018212 (2016).
44. Perdew, J. P., Burke, K. & Ernzerhof, M. Generalized gradient approximation made simple. *Phys. Rev. Lett.* **77**, 3865–3868 (1996).
45. Ikigaki, K., Okada, K. & Takahashi, M. Epitaxial growth of multilayered metal–organic framework thin films for electronic and photonic applications. *ACS Appl. Nano Mater.* **4**, 3467–3475 (2021).
46. Zhuang, J. L. et al. Insight into the oriented growth of surface-attached metal–organic frameworks: surface functionality, deposition temperature, and first layer order. *J. Am. Chem. Soc.* **137**, 8237–8243 (2015).

Acknowledgements

This work was supported by National Natural Science Foundation (NSFC) of China (grant nos. 52394170 and 52394174, Y.-S.H.; 22422906 and 92372116; X.R.; 52072370 and 92472201; J.Z.), Strategic Priority Research Program of the Chinese Academy of Sciences (grant no. XDA0400000; Y.-S.H.) and Beijing Natural Science Foundation (grant nos. JQ24006; X.R.; 2222078; J.Z.). We acknowledge N. Wu at the Center for Physicochemical Analysis and Measurements in ICCAS for solid-state NMR measurements.

Author contributions

Y.-S.H., X.R., Y. Lu and J.Z. designed and supervised the project. Y. Liu synthesized, characterized (XRD, IR, BET, SEM, EIS and LSV–GCMS) and electrochemically tested the samples and analysed the data with Q.Z., R.B. S.H., F.D., L.C. and X.R. X.C., S.W., C.Z., X.W. and F.W. performed the STEM measurements and analysis. H.M., C.Z. and Y. Liu designed and performed DFT calculations and analysis. C.Z. performed the TEM and electron energy loss spectroscopy measurements and analysis. Y. Liu, Y.X.L., X.R. and Y.-S.H. wrote the manuscript. All the authors participated in the discussion to improve the paper and made revisions of the whole manuscript.

Competing interests

The authors declare no competing interests.

Additional information

Supplementary information The online version contains supplementary material available at https://doi.org/10.1038/s41560-025-01857-y.

Correspondence and requests for materials should be addressed to Xiaohui Rong, Yaxiang Lu, Junmei Zhao or Yong-Sheng Hu.

Peer review information *Nature Energy* thanks the anonymous reviewers for their contribution to the peer review of this work.